International Journal of Heat and Mass Transfer 98 (2016) 176–182

Contents lists available at ScienceDirect

International Journal of Heat and Mass Transfer

journal homepage: www.elsevier.com/locate/ijhmt

Numerical study of gas mixture separation in curved nozzles

Tomás M. Guozden [a], Alejandro Clausse [b,*]

[a] CNEA and Instituto Balseiro, 7400 Bariloche, Argentina
[b] CNEA-CONICET and National University of Central Buenos Aires, 7000 Tandil, Argentina

ARTICLE INFO

Article history:
Received 29 October 2015
Received in revised form 11 February 2016
Accepted 4 March 2016

Keywords:
Curved nozzle
Species separation
Supersonic flow
Separative capacity

ABSTRACT

Species separation can be produced by imposing a pressure gradient in gaseous mixtures, which induces different molecular velocities depending on the molar weight. Pressure gradients can be achieved by centrifugal forces brought about by the passage of the gas through a curved nozzle at supersonic velocity. The efficiency of this process depends on the geometry of the nozzle as well as the flow operating conditions. The numerical solver Fluent was used in order to produce a model of the aerodynamics and the oxygen diffusion of a steady-state flow of air in a curved nozzle. The development of the pressure and O_2 concentration profiles along the nozzle were analyzed for different pressure boundary conditions at the inlet and the exit, testing several nozzle sizes. Optimum values of the cut and the inlet pressure were found which maximize the separation efficiency. The effect of the exit pressure was associated with the axial pressure distribution along the inner wall of the nozzle. The results were compared with measurements showing good agreement.

1. Introduction

It is well known that species separation can be produced by imposing a pressure gradient in gaseous mixtures, which induces different molecular velocities depending on the molar weight. A direct method to produce pressure gradients are centrifugal forces, which can be brought about by the passage of the gas through curved nozzles. This kind of processes are known as fixed-wall centrifuges, in contrast with the so-called centrifuge process, and have been widely studied in the 60's and 70's [1–4]. According to Stern et al. [5] the earliest proposal of separating gas mixtures in high velocity jets go back to P. Dirac during World War II and the concept was experimentally verified by Tahourdin in 1946. To the authors' knowledge, the first quantitative model of the process was presented by Sherman [6], where the mass diffusion in an aerodynamic field is separated in terms of concentration, pressure and temperature gradients, and volume forces.

Becker et al. [2] found that the optimum operating conditions of curved nozzles of different sizes leave approximately invariant the product of the inlet pressure times the diameter. Further pressure and size effects are also discussed in [1]. Similar scaling laws were suggested for free jets in which strong local pressure gradients are also generated by strongly curved streamlines [8–10]. In some of these systems, the experimental conditions extend to the free molecular regime, which invalidate the aerodynamic description. Molecular separation features of this regime, called Mach number focusing, are discussed in [11]. Li et al. [12] proposed that the aerodynamic separation of species can be enhanced by the formation of clusters. To model such cases, the continuum mechanical description should be complemented by appropriate particle descriptions.

Recently, there has been a renewed interest to use the current computational capabilities in gas separation processes of multicomponent flows [13–15], including laser assisted aerodynamics [26]. For curved nozzles, the numerical modeling has been proposed in the 80's by Vercelli [7] who used a finite difference scheme to solve the isotopic separation of UF_6; but otherwise there are no further reports in the open literature. In the present article a numerical model of the aerodynamics and the oxygen diffusion of a steady-state flow of air in a curved nozzle is presented. The solver Ansys Fluent [16,17] is used to implement the aerodynamic equations to calculate the velocity, pressure and temperature fields, and also the mass diffusion between nitrogen and oxygen. The results are compared with experimental measurements showing good agreement. Finally the development of the pressure and O_2 concentration profiles along the nozzle for different boundary conditions at the inlet and the exit, for several nozzle sizes, is analyzed to identify scale effects.

2. Experimental setup

In order to have a reference to compare with, an experimental test nozzle designed to operate with air at low pressure conditions

* Corresponding author.
E-mail address: clausse@exa.unicen.edu.ar (A. Clausse).

http://dx.doi.org/10.1016/j.ijheatmasstransfer.2016.03.015
0017-9310/

was constructed. Figs. 1 and 2 show a photograph of the nozzle and a diagram of the experimental setup. The outlet flows Q_L and Q_P discharge in a single buffer chamber which is vacuumed by means of a Root mechanical pump at a flow rate of 210 m^3/h. The outlet pressure P_b (2.0 ± 0.1 mbar) is measured before the buffer with a pirani-gauge type manometer. The inlet pressure P_o (52 ± 1 mbar) is measured by a capacitive absolute manometer and it is controlled by tuning valve A.

To determine the change in concentration of oxygen and nitrogen, gas samples are collected from the inlet flow and the outlet flow Q_L, which is depleted in oxygen. The samples are stored in a flexible vessel containing approximately 5000 cc at ambient pressure. The oxygen concentration of each sample is measured with an electrochemical analyzer Siemens ULTRAMT 23. The experiment was repeated three times, obtaining an average depletion in oxygen of (0.10 ± 0.01)%. The results are shown in Table 1.

3. Numerical model

The aerodynamics of the nozzle was modeled using a 2D approximation neglecting the effects of the lateral walls. The inner curved wall is described by a circular arc of radius 7.2 mm, whose center is taken as the origin of coordinates. The external wall is described by a circular arc of radius 10.4 mm centered at the point (1.4 mm, 0.7 mm). A mesh of 3858 quadrilaterals was taken as the base reference, which then was subsequently refined to ensure numerical convergence (Fig. 3). The minimum orthogonal quality and the maximum aspect ratio of the meshes, determined using the capabilities of the software [20], are listed in Table 2.

The equations of compressible fluid in stationary state were numerically solved with the code Ansys-Fluent, which is based in the finite volume method with the gas density taken as an independent variable within the flux-difference-splitting scheme [18,19]. Turbulence models were not included because the residence time of the fluid through the process is not enough to trigger this regime.

The mean molecular mass of the air was taken as 28.97 g/mol. A linear dependence with the temperature was assumed for the thermal conductivity. The temperature dependence of viscosity and specific heat was taken from the data provided by the solver. The functions were compared with the experimental data reported by Bergman et al. [20] showing good agreement (Fig. 4). Constant pressure boundary conditions were imposed at the inlet and the outlets, although the exit pressure is used only when the exit flow is subsonic. At the curved walls null velocity and constant temperature conditions are imposed.

The convergence of the numerical calculation was tested increasing the refinement of the mesh. Fig. 5 shows the evolution of the residual errors relative to the initial condition for each mesh detailed in Table 2. It can be seen that the final error, <10^{-13}, is the same in all cases. Moreover, the number of iterations required to achieve convergence increases with the square root of the mesh size, which is consistent with the finite volume method.

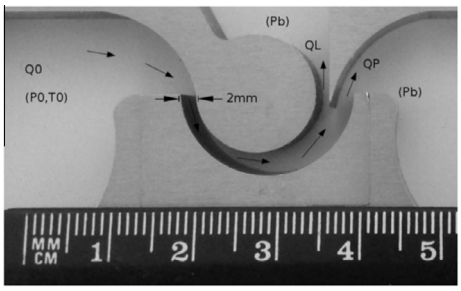

Fig. 1. Photograph of the curved nozzle showing the inlet flow rate Q_o, the inlet and exit pressures P_o and P_b, the inlet temperature T_o, exit flow rates Q_L and Q_P.

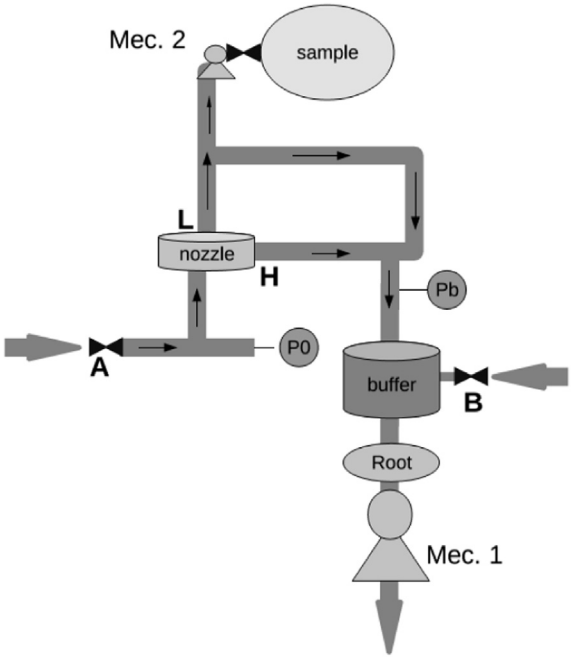

Fig. 2. Diagram of the experimental setup.

Table 1
Measured oxygen concentration.

Sample	Inlet (%)	Outlet (Q_L) (%)
1	20.98	20.89
2	20.92	20.83
3	21.01	20.92

The solution of the aerodynamic problem provides the mechanical and thermal fields, *i.e.*, velocity, pressure and temperature, which controls the diffusion between species. In the absence of external forces such as electromagnetic fields, the diffusion between gas species is driven by concentration, pressure and temperature gradients. The diffusion velocity between species is then given by [21]:

$$u_1 - u_2 = -\frac{n^2}{n_1 n_2} D_{12}\left[\nabla c_1 + \frac{n_1 n_2 (m_1 - m_2)}{n\rho}\frac{\nabla P}{P} + k_T \frac{\nabla T}{T}\right] \quad (1)$$

where n_i, u_i and m_i are the number density, relative velocity respect to the average velocity of the mixture, and molecular mass of the species i, D_{12} is the diffusion coefficient, and:

$$n = n_1 + n_2 \quad (2)$$

$$\rho = n_1 m_1 + n_2 m_2 \quad (3)$$

Assuming a reference frame moving with the mean velocity of the mixture, u_1 and u_2 satisfy:

$$n_1 u_1 + n_2 u_2 = 0 \quad (4)$$

The diffusion flux of oxygen, $J_1^D = n_1 u_1$, is then given by:

$$J_1^D = -n D_{12}\left[\nabla c_1 + \frac{n_1 n_2 (m_1 - m_2)}{n\rho}\frac{\nabla P}{P} + k_T \frac{\nabla T}{T}\right] \quad (5)$$

In the laboratory reference frame the total flux of oxygen J_1 is given by:

Fig. 3. Perimeter of the nozzle (left), original mesh (center), first refinement (right).

Table 2
Mesh parameters.

Mesh	1	2	3	4
Number of elements	3858	15,432	61,728	246,912
Max. aspect ratio	3.0	3.0	3.1	3.4
Min. orthogonal quality	0.9	0.9	0.9	0.9

$$J_1 = J_1^D + n_1 u \tag{6}$$

where u is the velocity of the mixture.

The diffusion coefficient D_{12} depends on the local pressure P according to [22]:

$$D_{12} = D_o \frac{P_o}{P}\left(\frac{T}{T_o}\right)^{1.823} \tag{7}$$

where $D_o = 0.181$ cm^2/s, $P_o = 1$ atm and $T_o = 343$ K. The local values of u, P and T are given by the aerodynamic solution.

The convection–diffusion problem defined by the flux J_1 was solved using the user defined scalar and user defined functions options of the Fluent code [23]. The inlet oxygen concentration was fixed at 0.21. In case of recirculation at the outlets, only convection transport is allowed with boundary condition $n_1 = 0.21$.

4. Results

The model described in the previous section was applied to calculate the flow established in the curved nozzle represented by mesh 3, under the experimental operating conditions, that is, inlet and exit pressure 52 mbar and 2 mbar, respectively. Fig. 6 show the maps of velocity, pressure, temperature and molar fraction of O_2. It can be seen that the transversal radial profiles of all the variables start developing about the mid run section. The maximum velocities at the end of the run are about 500 m/s close to the center line. The radial pressure gradient can be clearly visualized along the second half of the run. The maximum relative gradient, $(1/p)(dp/dr)$, is about 0.9 mm^{-1} at the radial position $r = 8.6$ mm. The temperature, in turn, drops along the run due to the flow expansion, reaching cold spots about 110 K. The oxygen concentration develops a radial gradient driven by the pressure gradient, in agreement with Eq. (5) .

In order to assess the numerical error of the concentration results, a diffusion case turning off the pressure diffusion term was calculated, giving a maximum O_2 concentration difference of 1.3×10^{-6}.

Fig. 7 shows the exit profiles at the nozzle exit of the four variables. A numerical estimation of the measured depleted concentration of oxygen can be calculated by integrating the molar flow of oxygen over the flow collected on the inner section of the exit divided by the total flow. The resulting value is 0.2081 ± 0.0005. The confidence band was assessed taking into account the uncertainties in the input parameters, mainly the sensitivity to the mesh, the pressure and temperature boundary conditions, and the construction geometric tolerances. This value should be compared with the measurement, 0.2088 ± 0.0004. The slight over estimation of the oxygen depletion can be attributed to the 2D approximation that neglects the effects of the boundary layer on the closing lateral walls.

The oxygen concentration distribution inside the nozzle can be better appreciated in Fig. 8, which shows the development of the concentration profile at different cross sections of the flow. It can be seen that although there is a concentration difference between the inner and the outer border of the nozzle that grows as the fluid advances, the concentration at the midsection of the channel remains unperturbed. The width of this region progressively narrows toward the end of the run. A similar behavior can be observed in the velocity profile, whose development along the run is shown in Fig. 9. The scenario is a typical case of flow with Schmidt number close to unity, where the momentum and mass diffusivities are similar. Actually, the Schmidt number for air at the conditions of the experiment is about 0.7, slightly dependent on the temperature but independent on the pressure. The inlet pressure, however, does have a direct influence in the development length of all the flow variables. Figs. 10 and 11 show the exit profiles of the velocity and the oxygen concentration, obtained imposing different inlet pressure conditions. As inlet pressures decrease, the diffusion

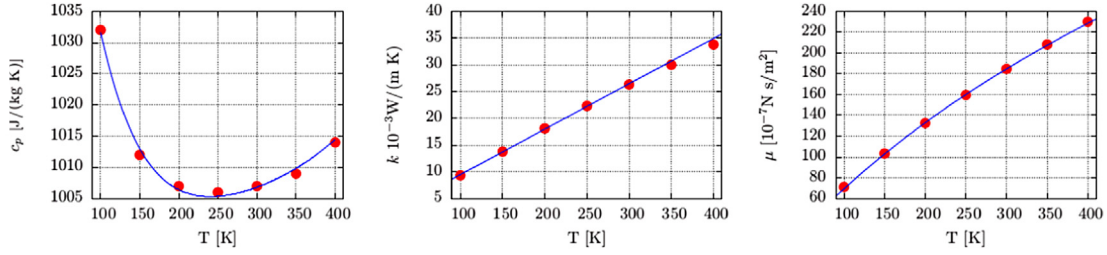

Fig. 4. Fitting of the air properties, specific heat (left), thermal conductivity (center), dynamic viscosity (right). Experimental data (points) and fitted correlations (solid curves).

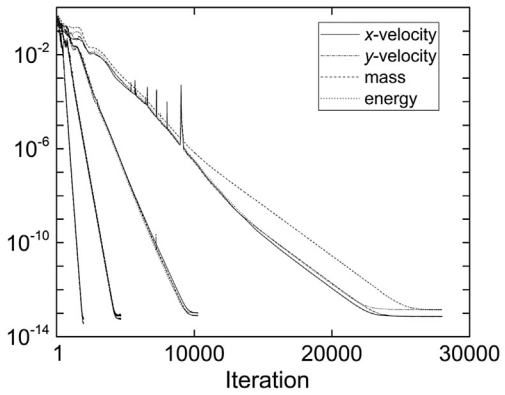

Fig. 5. Evolution of residuals for each mesh defined in Table 2.

dynamics becomes faster for both molar fraction and momentum, thus shortening the development length. We can see this for pressures lower than 12 mbar, where the diffusion of momentum and molar fraction at the exit are completely developed. In turn, higher inlet pressures yield greater velocities, which produce higher pressure gradients. Fig. 12 shows the profile of the relative pressure gradient, $(1/p)(dp/dr)$, at the nozzle exit. This is the driving force of the pressure gradient term in Eq. (5). It can be seen that, as the pressure decrease, the radial position of the maximum moves toward the center line of the cross section, albeit the value of the maximum decreases.

Since the velocity and concentration profiles at the exit are strongly influenced by the inlet pressure, one would expect that the separation capacity of the nozzle will also change with the inlet pressure. In order to assess the nozzle as an enrichment device, we will analyze the nitrogen enrichment on the inner side. Accordingly, the nitrogen concentration and velocity profiles were calculated for a range of inlet pressures between 2 and 52 mbar, and the inlet flow Q_o, the inner-exit flow Q_L and the molar inner-exit oxygen concentration c_L, are calculated for each pressure. The cut θ and the separation factor α for nitrogen are then given by [24]:

$$\theta = \frac{Q_L}{Q_o} \tag{8}$$

$$\alpha = \left(\frac{1-c_L}{c_L}\right) \Big/ \left(\frac{1-c_o}{c_o}\right) \tag{9}$$

where c_o is the inlet concentration of oxygen.

Fig. 13 shows the dependence of α and θ with the inlet pressure. It can be seen that the cut θ decreases as the pressure increases. This is due to the increase of the pressure gradient, which reduces the gas density on the inner side. Moreover, there is an optimum pressure for which the separation factor is maximum, around 10 mbar, which is approximately in the same range of pressures where complete flow development is achieved. It is reasonable to expect that the optimum pressure for maximum α will be different for other partitions of the exit section. The detailed calculation of other nozzles would require the impractical task of generating and calibrating numerous meshes. However, an approximate assessment can be done by modeling a nozzle without exit partition and then calculating α assuming that the presence of the blade does not affect significantly the results. In Fig. 13 the results of the calculations with and without blade, which are compared showing good agreement within 6%, and 3% close to the maximum.

Using the fields calculated with a mesh of a nozzle without blade, the separation factor was calculated as a function of the inlet pressure and the position of a hypothetical exit partition. Fig. 14 shows the resulting contour map. As can be seen, the separation factor is maximum when the flow is cut closer to the inner side, which is reasonable since the radial gradient of the nitrogen concentration (the light species) is negative. However, it should be noted that the closer the partition is to the inner border the lower is the collected flow. Hence, the parameter that better assess the optimum partition is the separative capacity, Δ, which gives the

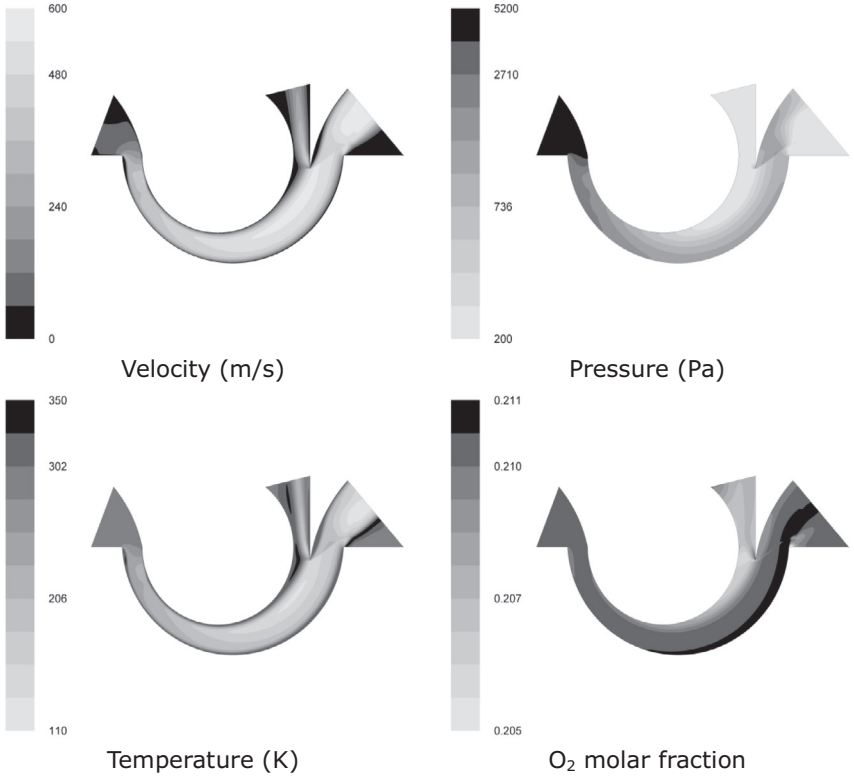

Fig. 6. Contour maps of the velocity, pressure, temperature and oxygen concentration. The inlet and outlet pressure are 52 and 2 mbar, respectively.

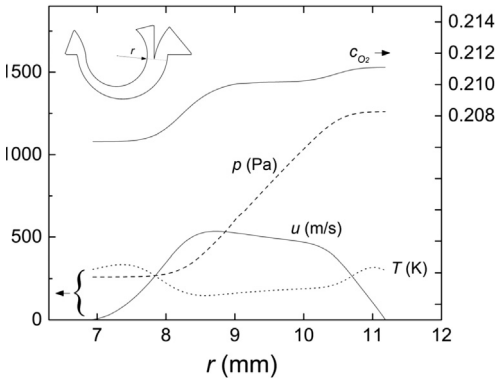

Fig. 7. Radial profiles at the exit section of the nozzle before the flow splitter (dashed section in the upper left sketch).

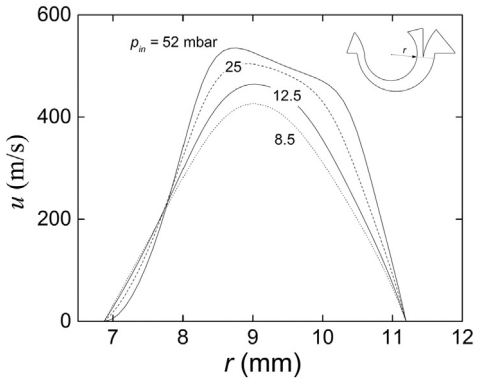

Fig. 10. Velocity profile obtained for different inlet pressures at the nozzle exit before the flow splitter (dashed section in the upper right sketch).

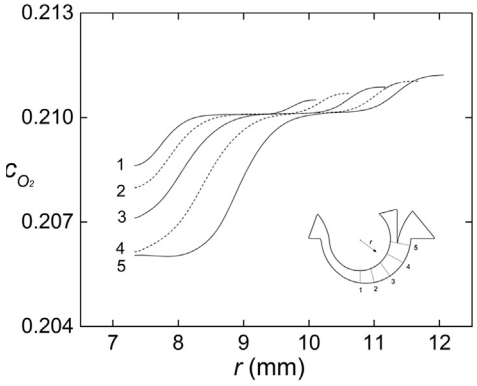

Fig. 8. Development of the oxygen concentration profile (inlet pressure: 52 mbar).

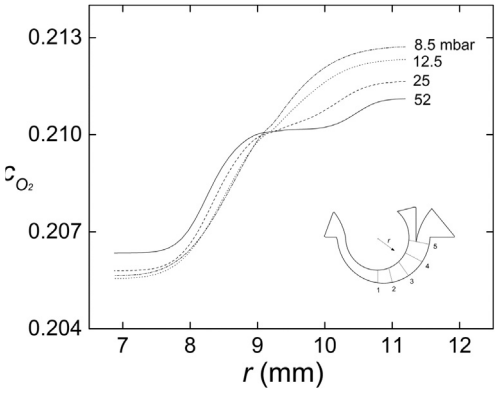

Fig. 11. Oxygen concentration profile at the nozzle exit (section 5) obtained for different inlet pressures.

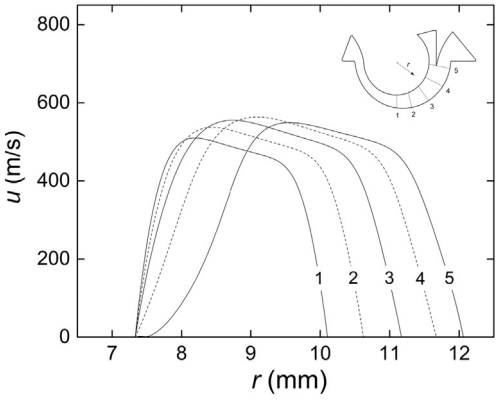

Fig. 9. Development of the velocity profile (inlet pressure: 52 mbar).

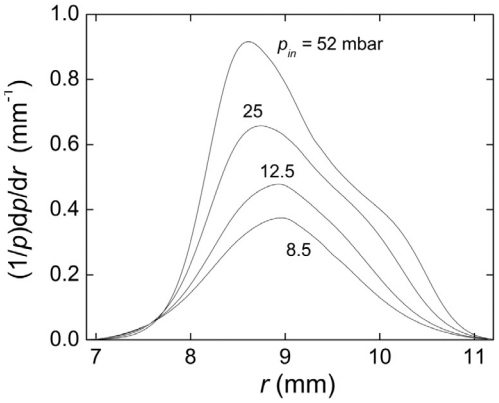

Fig. 12. Exit profile of the pressure-gradient diffusion term obtained for different inlet pressures.

kg of separative work units (SWU) per kg of inlet mixture, and is given by [25]:

$$\Delta = \frac{1}{2}\theta(1-\theta)(\alpha-1)^2 \tag{11}$$

Fig. 15 shows the contour map of Δ. Interestingly, the results indicate that there is an optimum design locating the partition in the exit cross section at a radius 8.75 mm and operating at 6 mbar inlet pressure. These magnitudes should be taken as a guide since the presence of the blade can change to some extent the exact values.

As long as the flow is supersonic the total flow rate is determined only by the inlet pressure, independently of the exit pressure boundary condition. However, the latter should be low enough as to ensure supersonic conditions along the whole run, otherwise those conditions might be compromised affecting the flow and the concentration. To study this, a sensitivity analysis of the influence of the exit pressure on the separation process was performed, keeping the inlet pressure and the exit partition at the reference values (52 mbar and 8.5 mm). Fig. 16 shows the variation of the separation factor α for different exit pressures. Interestingly, α increases as the exit pressure increases up to an optimum value at 2.67 mbar. This feature can be explained by

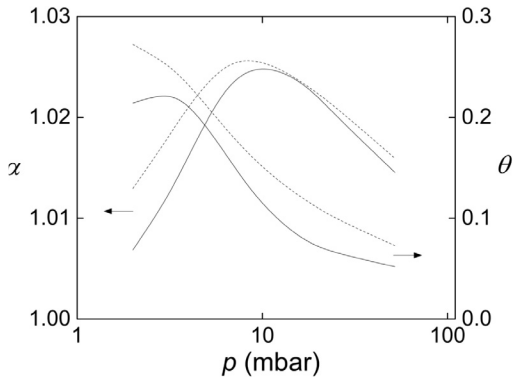

Fig. 13. Dependence of the separation factor α and the flow cut θ with the inlet pressure, calculated including the blade in the geometry (solid) and estimated from the profiles calculated without blade (dashed).

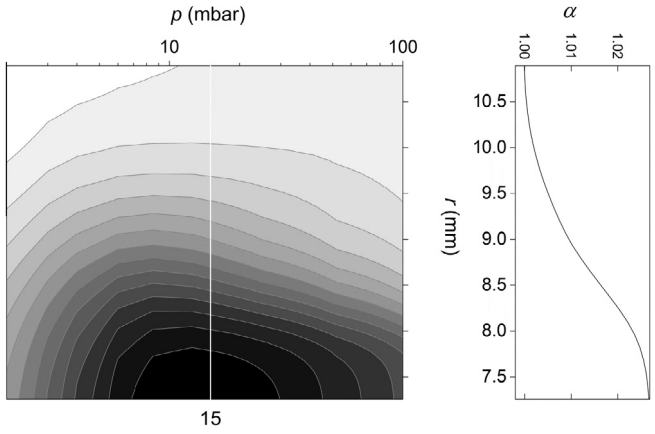

Fig. 14. Variation of the separation factor α with the position of the exit partition, r, and the inlet pressure, p.

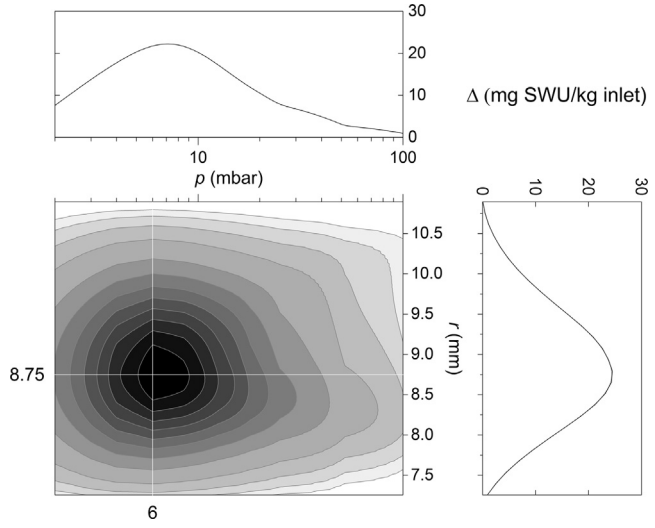

Fig. 15. Variation of the separating capacity with the position of the exit partition, r, and the inlet pressure, p.

analyzing the pressure along a current line adjacent to the inner border, as shown in Fig. 17. The graphic shows the progressive decrease of the pressure along the inner wall for different exit pressures p_b. The inner-wall pressure decreases monotonically along the nozzle run until a point near the exit, from where it increases until the exit partition. This feature is caused by the flow restriction produced by the blockage of the blade. After the partition the pressure progresses to the exit pressure. Also it can be seen that, provided that $p_b < 2$ mbar, the pressure on the inner wall upstream the blade is not affected by the outlet pressure, whereas for p_b between 2 and 3 mbar the inner-wall pressure is altered producing an earlier separation of the boundary layer and recirculation effects. The increase of α is explained by the reduction of the inner exit flow rate, as can be seen in the variation of the cut θ shown in Fig. 16. The lower flow rates are produced by lower inner velocities, which increase the residence time and therefore increase the concentration gradient. However, once the boundary layer is separated the pressure gradient decreases (see the inner-outer pressure difference in Fig. 17), which ultimately deteriorates the diffusion driving force and the separation factor.

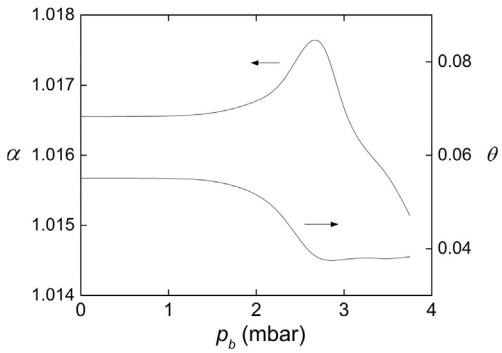

Fig. 16. Influence of the exit pressure p_b on the separation factor and the flow cut.

5. Conclusions

A numerical 2D model of the aerodynamics and the oxygen diffusion of a steady-state flow of air in a curved nozzle was used to calculate the change in the concentration of oxygen and nitrogen at the outlet. The results were compared with experimental measurements showing good agreement. The development of the pressure and O_2 concentration profiles along the nozzle were analyzed for different pressure boundary conditions at the inlet and the exit. Optimum values of the cut and the inlet pressure were found which maximize the separation efficiency. The effect of the exit pressure was associated with the axial pressure distribution along the inner wall of the nozzle.

It is worth noting that the diffusion flux given by Eqs. (5) and (7) is invariant to the product of the pressure times the length scale. In effect, the three terms between brackets in Eq. (5) scale with the inverse of the length whereas, for a given temperature, Eq. (7) scales with the inverse of the pressure. Therefore, the flux J_1^D is invariant provided that the product of the pressure times the length scale is conserved. Moreover, this invariance holds also for the Reynolds number for ideal gases. In effect, for ideal gases the sonic velocity u_s and the dynamic viscosity μ depend solely on the temperature. Therefore, inasmuch as the gas density ρ is proportional to the pressure, the Reynolds number, $u_s L\rho/\mu$, scales with pressure times length scale. Hence, the invariance extends to the aerodynamics results, for in the present study turbulence effects are neglected, and so the flow is characterized solely by the Reynolds number. Therefore, the present results are invariant to the mentioned product, which in practical terms boils down to the inlet pressure (which determines the pressure level in the nozzle) times the nozzle radius (which determines the length scale for a given aspect ratio). This important feature was numerically verified and holds while the gas behavior is ideal. However, at very low pressures the Knudsen number approaches unity, invalidating

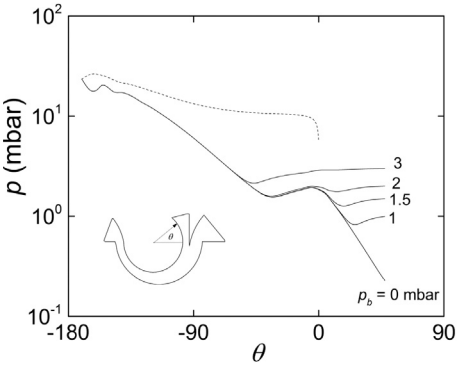

Fig. 17. Pressure profile along the inner (solid) and outer (dash) borders, for different exit pressures. The outer profile is not influenced by the exit pressure p_b.

the continuum hypothesis. In this range, particle dynamics methods can be of interest to study the transition to the free molecular regime, and in particular the influence of clusters formations in aerodynamic molecular separation [26].

Acknowledgments

The authors want to thank INVAP and the LASIE project group of the Argentine Atomic Energy Commission for its collaboration in the experiment.

References

[1] A. Kogan, Separation of a gas mixture in curved supersonic flow, Int. J. Heat Mass Transfer 9 (1) (1966) 1–10.
[2] E.W. Becker, K. Bier, W. Bier, R. Schutte, D. Seidel, Separation of the isotopes of uranium by the separation nozzle process, Angew. Chem. Int. Ed. 6 (6) (1967) 507–518.
[3] E.W. Becker, W. Bier, W. Ehrfeld, K. Schubert, R. Schfitte, D. Seidel, Uranium enrichment by the separation-nozzle process, Naturwissenschaften 63 (1976) 407–411.
[4] E.W. Becker, The separation nozzle process for enrichment of Uranium-235, Prog. Nucl. Energy 1 (1977) 27–39.
[5] S.A. Stern, P.C. Waterman, T.F. Sinclair, Separation of Gas mixtures in a supersonic jet. II. Behavior of helium-argon mixtures and evidence of shock separation, J. Chem. Phys. 33 (3) (1960) 805–813.
[6] F. Sherman, Hydrodynamical theory of diffusive separation of mixture in a free jet, Phys. Fluids 8 (1965) 773–779.
[7] P. Vercelli, Modelagem numérica do processo de enriquecimento bocal de separacao, Com. Nac. Energ. Nuclear (M.Sc. thesis), 1983. INIS-BR363, S. Paulo, Brazil, 99p, http://www.iaea.org/inis/collection/NCLCollectionStore/_Public/16/067/16067052.pdf, (in Portuguese)..
[8] P.C. Waterman, S.A. Stern, Separation of gas mixtures in a supersonic jet, J. Chem. Phys. 31 (2) (1959) 405–419.
[9] V.H. Reis, J.B. Fenn, Separation of gas mixtures in supersonic jets, J. Chem. Phys. 39 (12) (1963) 3240–3250.
[10] S.A. Stern, P.C. Waterman, T.F. Sinclair, Separation of gas mixtures in a supersonic jet, behavior of helium-argon mixtures and evidence of shock separation, J. Chem. Phys. 33 (3) (1960) 805–813.
[11] P.K. Sharma, E.L. Knuth, W.S. Young, Species enrichment due to Mach number focusing in a molecular beam mass spectrometer sampling system, J. Chem. Phys. 64 (11) (1976) 4345–4351.
[12] W. Li, M.J. Stirniman, S.J. Sibener, The effect of cluster formation on mass separation in binary molecular beams, J. Chem. Phys. 112 (7) (2000) 3208–3213.
[13] T. Farouk, B. Farouk, A. Gutsol, Simulation of gas species and temperature separation in the counter-flow Ranque–Hilsch vortex tube using the large eddy simulation technique, Int. J. Heat Mass Transfer 52 (2009) 3320–3333.
[14] N. Alkhamis, D.E. Oztekin, A.E. Anqi, A. Alsaiari, A. Oztekin, Numerical study of gas separation using a membrane, Int. J Heat Mass Transfer 80 (2015) 835–843.
[15] N. Alkhamis, A.E. Anqi, A. Oztekin, Computational study of gas separation using a hollow fiber membrane, Int. J. Heat Mass Transfer 89 (2015) 749–759.
[16] Ansys®, Academic research, Release 13.0, ANSYS Inc., 2013.
[17] Ansys®, Fluent user's guide, ANSYS Inc., 2013.
[18] P.L. Roe, Characteristic based schemes for the Euler equations, Annu. Rev. Fluid Mech. 18 (1986) 337–365.
[19] Ansys®, Fluent theory guide, ANSYS Inc., 2013.
[20] T. Bergman, A. Lavine, F. Incropera, D. DeWitt, Fundamentals of Heat and Mass Transfer, sixth ed., 2007. New York, NY.
[21] S. Chapman, T.G. Cowling, The mathematical theory of non-uniform gases, Cambridge University Press, 1970.
[22] R. Byron Bird, E. Warren, E.N.L. Stewart, Transport Phenomena, John Willey & Sons Inc., 2002.
[23] Ansys®, Fluent UDF manual, ANSYS Inc., 2013.
[24] K. Cohen, The theory of isotope separation as applied to the large scale production of U235, Mc Graw Hill, 1951.
[25] M. Benedict, T. Pigford, H.W. Levi, Nuclear Chemical Engineering, McGraw Hill, 1981.
[26] J.W. Eerkens, J. Kim, Isotope separation by selective laser-assisted repression of condensation in supersonic free jets, AIChe J. 56 (2010) 2331–2337.